

Instrument Science Report WFC3 2013-04

WFC3/IR Internal Flat Fields

Tomas Dahlen

March 20, 2013

ABSTRACT

We report on the investigation of the WFC3 IR channel internal flat field images taken during Cycles 17, 18, and 19 using the Tungsten #2 calibration lamp. To complement this data, we also include observations taken during the Thermal Vacuum 3 testing on ground and the Servicing Mission Observatory Verification 4 program. Between the on ground testing in 2008 and the on orbit measurements starting 2009, we find an increase in the lamp flux of about ~8%, consistent with previous investigations. For the on orbit observations, we find that the lamp intensity has been stable within 0.4% during the time between SMOV4 (July 2009) and Cycle 19 (September 2012) and between different filters. This scatter is, however, larger than expected from pure Poisson statistics. Possible systematic effects contributing to the scatter include variations in the flat field lamp flux, effects due to image persistence and systematic effects due to an excessive flagging of pixels as being hit by cosmic rays in the up-the-ramp fitting. We do not find any significant change in the illumination pattern between the three Cycles. We do possibly detect some small differences in the response in the pixels certain areas in the bottom right of the detector (e.g., pixels affected by the wagon wheel feature and other artifacts). The illumination pattern from the internal flat field lamp is significantly different from that expected from actual science images. The internal flat field images are therefore not well suited for creating flat field files to be used in the calibration of IR data.

Introduction

The WFC3/IR internal flat field calibration program studies the stability and structure of the flat field images taken through all filter elements in the WFC3-IR channel. Flat fields are monitored to capture any overall temporal trends in the count rates of the flat fields, which could be a sign of an overall change in the detector QE or, more likely, a change in the intensity of the internal flat field calibration lamp. The high signal-to-noise observations also provide a map of the pixel-to-pixel flat field structure, which is used to detect any significant change in the response of individual pixels. These latter results are used to monitor the number of pixels that are flagged as bad pixels. Also, the pixel-to-pixel flat field structure can be used to identify the positions of any dust particles.

In principle, internal flat field images could also be used to produce high signal-to-noise flat field calibration files to be used by the WFC3 image calibration software. However, tests show that the illumination pattern between the internal flat field images and on orbit science observations are sufficiently different to produce significant biases in photometry if the internal flat fields were to be used when calibrating images. Instead, a combination of a large number of sky images was used to produce the flat field calibration files that are used by the calibration software (Pirzkal et al. 2011).

IR Internal Flat Field Calibration Programs

Here we present the results of the internal flat field programs conducted during HST Cycles 17 through 19 (August 2009 to September 2012). The covered programs are 11915 (Cycle 17; P.I.: P. McCullough), 12338 (Cycle 18; P.I.: A. Viana), and 12712 (Cycle 19; P.I.: T. Dahlen). The numbers of internal orbits used in the three programs are 150, 58, and 33, respectively. During these program, the five broad band filters F105W, F110W, F125W, F140W, and F160W, were monitored during approximately eight to ten epochs during Cycle 17 and 18, and somewhat less frequent, about six epochs, during Cycle 19. At each epoch, at least three individual exposures were taken. The remaining ten narrow and medium band filters (F098M, F126N, F127M, F128N, F130N, F132N, F139M, F153M, F164N, and F167N), were also monitored regularly during Cycle 17. During Cycle 18 and 19, these filters were only observed once with two to three exposures taken in the middle of each cycle. The observations were taken using the internal Tungsten lamp #2 with exposure times sufficient to reach 50,000 - 60,000 electrons per pixel. These high counts should result in Poisson noise of an individual pixel and a single exposure of about 0.5%, comparable to or smaller than any individual astronomical image made by WFC3 IR. Adding multiple exposures further brings down the noise per pixel. In Table 1, we summarize the observations listing the total number of exposures, exposure times, sampling sequences and achieved counts and count rates, for the different filters. The table shows that the mean counts per pixel is $>50,000e^-$ for all

filters, assuring sufficient Poisson statistics.

Table 1. Observational Summary

Filter	N(Cy17)	N(Cy18)	N(Cy19)	exp. time (s)	Samp seq.	Nsamp	e-/pix	e-/pix/s
Broad band monitoring filters								
F105W	22	39	20	82.94	SPARS10	9	58470	705
F110W	36	39	20	38.12	RAPID	13	58140	1525
F125W	44	39	20	52.94	SPARS10	6	58970	1114
F140W	30	39	20	38.12	RAPID	13	61360	1610
F160W	66	39	20	52.94	SPARS10	6	59470	1123
Narrow and medium band filters								
F098M	22	3	2	202.93	SPARS50	5	62470	308
F126N	22	3	2	1002.93	SPARS100	11	53030	52.9
F127M	22	3	2	202.94	SPARS25	9	57040	281
F128N	22	3	2	902.93	SPARS100	10	55170	61.1
F130N	22	3	2	902.93	SPARS100	10	58560	64.9
F132N	22	3	2	902.93	SPARS100	10	57290	63.4
F139M	44	3	2	202.93	SPARS50	5	50454	249
F153M	22	3	2	202.94	SPARS25	9	57230	282
F164N	22	3	2	802.93	SPARS100	9	55100	68.6
F167N	22	3	2	802.93	SPARS100	9	57551	71.7

Notes: **The table lists the number of internal flat field exposures per filter during HST Cycles 17, 18, and 19. For each filter the exposure time, sampling sequence, number of samples, the average electron per pixel and electron per pixel per second are also given.**

Results

Temporal evolution of the count rates

To examine if there are any temporal variations in the detected count rates, we calculate the median count rate in each of the five broad band filters for the three HST Cycles. In addition, we make use of the existing internal flat field exposures from July 2009 taken during the Servicing Mission Observatory Verification 4 (SMOV4) program 11433 (Hilbert 2009) and the internal flat fields produced on ground during Thermal Vacuum Test 3 (TV3) in spring of 2008 (Bushouse 2008).

Figure 1 shows the count rates, with mean normalized to unity, for the five broad band filters as a function of time including TV3, SMOV4 and HST Cycles 17 through 19 internal flat field images. The figure shows a brightening of the Tungsten #2 lamp by ~8% between the ground based and space based observations. This is consistent with the results of Hilbert (2009) who found a brightening of 6-10% in the IR channel. A similar brightening of the Tungsten lamps #1 and #3 was also reported for the UVIS internal flat

field taken during SMOV4 (Baggett et al. 2009). Contributing to this effect is likely that the lamps are hotter in space due to the deeper vacuum, which makes the lamps less heat sunk compared to the ground testing (Powers 2013).

The on orbit data, covering SMOV4 to Cycle 19, show no significant evolution in the detected count rate with time. Therefore the flux of the Tungsten internal lamp appears to have been stable since SMOV. We do, however, note that the statistical error bars of the data points in Figure 1 are smaller than the size of the symbols, typically $<0.1\%$. Therefore, the scatter between observations seen in the figure, which has an rms of $\sim 0.4\%$, has to be attributed to systematic effects. Included in the possible systematic effects are 1) variations in the lamp flux, 2) image persistence effects, 3) systematic effects in the up-the-ramp fitting. Below we comment on each of these possibilities.

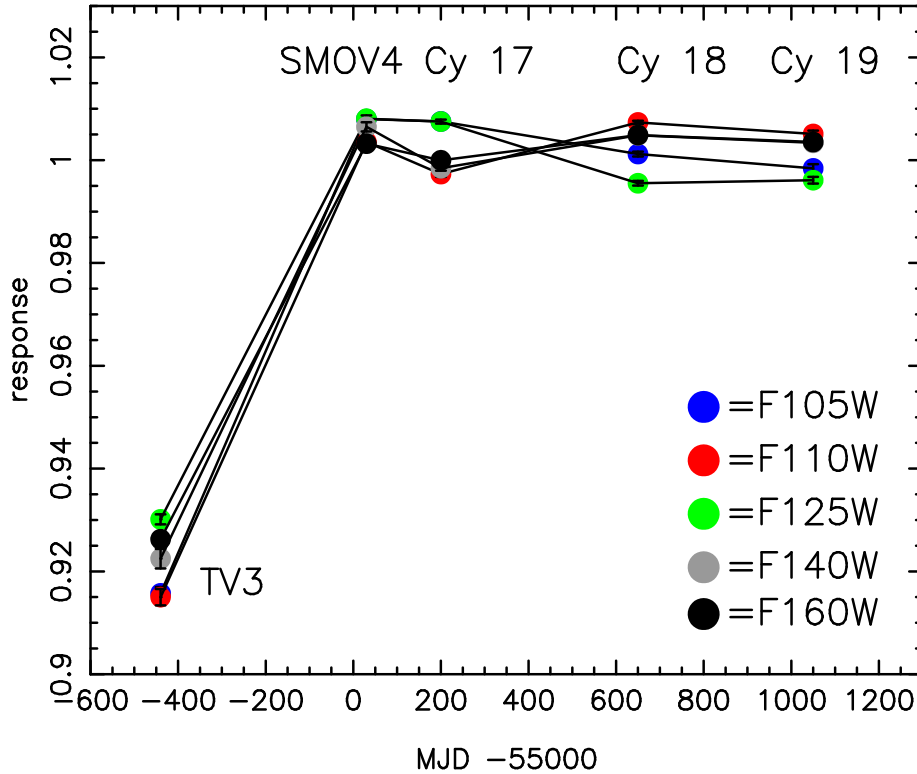


Figure 1. Relative detector count rates for internal flats illuminated with the Tungsten lamp in five different filters during five epochs; Thermal Vacuum Test 3 (TV3), SMOV4, and HST Cycles 17 to 19. There is a $\sim 8\%$ increase in the lamp intensity between the ground based and space based observations.

Variations in the lamp flux

Hilbert (2009) reported that the lamp flux during SMOV4 showed an image-to-image variation with an rms of $\sim 0.3\%$. For our Cycle 17 to 19 observations, we find a very similar rms in the range $0.2\text{-}0.4\%$, somewhat varying with cycle and filter. Therefore, variations in the Tungsten lamp flux could cause some of the scatter seen between the on orbit data points in Figure 1. However, since each data point is the mean of at least 20 individual measurements, one would expect an error in the mean of at most $0.4\%/\sqrt{20} \sim 0.1\%$ between Cycles and filters. The measured rms is larger than this, suggesting that additional systematic effects are in play.

Image persistence

The WFC3 IR detector exhibits image persistence in the sense that pixels that are filled to more than half of saturation will show a residual signal in subsequent images after the detector has been read out (Long et al. 2011). With the internal flat field images having typical counts of 55,000 e/pix and the full well is $\sim 78,000$ e, we do expect to experience some degree of image persistence in the internal flat field exposures. In general, the first exposure in each visit should be persistence free, while the subsequent observations may be affected. During the Cycle 18 and 19 observations, the five broad band filters were observed in the same order in each visit, i.e., F105W followed by F110W, F160W, F125W, and finally F140W. If there were any effects due to persistence, then the different filters would be affected in a similar way in these two Cycles. The fact that the relative ordering of the signal of these five filters in Cycle 18 and 19 is the same in Figure 1 is consistent with this. In Cycle 17, a different relative ordering of the filters was used. For example, the F110W and F140W filters were always observed first in the Cycle 17 visits, but later in the visit in Cycle 18 and 19. Figure 1 shows that the latter Cycle points for these filters are higher than the Cycle 17 points, indicating that persistence may have elevated the Cycle 18 and 19 points. Similarly, F105W was observed first in the Cycle 18 and 19 visits, but as the second filter in Cycle 17. Again, the count rate from F105W is higher in Cycle 17 than the two following Cycles, indicating that the former has been affected by persistence. The mean count rates for these filters are $0.6\text{-}0.9\%$ lower in the first exposure of the visit compared to later exposures. For the two remaining filters, F125W and F160W, there is no single pattern of the ordering within visits, these filters have been observed multiple positions and it is therefore difficult to draw any firm conclusion based on the figure. To investigate this further, we have taken a closer look at the Cycle 17 observations of F160W. For this filter, we have 66 exposures of which 22 are observed in the beginning of a visit, while the remaining are observed later within the visit and may therefore be affected by persistence. Consistent with the results above, we find that the images that are executed as the second or later exposure in the orbit have a count rate that is 0.7% higher than in the exposures at the beginning of the visit. This further suggests that persistence contribute to the scatter seen in Figure 1.

Systematic effects in the up the ramp fitting

The calibration software calwf3 calculates the count rates for each individual pixel in the IR detector by fitting a straight line to all the readouts in the up-the-ramp sampling. In this process, the calibration software can detect and exclude reads that deviates more than some given sigma threshold from the expected linear growth of the counts with time (in the non saturated linear region of the detector well). A cosmic ray (CR) hitting a pixel between two readouts, causing a jump in the counts, can therefore be flagged and the signal from the CR can be rejected. The number of CR hitting the IR detector is of the order 10 CR/s. For normal exposure times and typical CR incidences, less than 1% of the detector pixels should be affected by CRs.

For pixels with high count rates (>100 counts/s) observed with the SPARS sampling sequence, a significantly higher fraction of pixels are flagged as being hit by a CR compared to what is expected (T. Dahlen et al. 2013, in preparation). These apparently ‘false’ CR flags affect the count rate calculated in the up-the-ramp fitting by the calwf3 software in the sense that the pixel that has a ‘false’ CR flagged is assigned a count rate that is on average 0.5% lower compared to the case when it is not flagged as a CR hit pixel. Since the broad band internal flat-fields have count rates in excess of 300 counts/s, we do expect to see this effect in these images.

In Figure 2, we show the fraction of pixels that are flagged as being hit by CRs for the five broad band filters used for the internal flat field program. It is clear that the filters for which the SPARS sampling sequences were used have significantly higher CR fraction compared to what is expected. For F125W, more than 20% of the pixels are flagged in Cycle 18 and 19, compared to the expected $<0.1\%$ from true CRs. Since the falsely flagged pixels have a lower count rate compared to the non-flagged pixels, there should be a bias in the case where different numbers of pixels are flagged during different cycles. The high fraction of CR hit pixels in F125W for Cycle 18 and 19 is consistent with the relatively lower counts in these cycles seen in Figure 1.

Fraction CR in internal flats

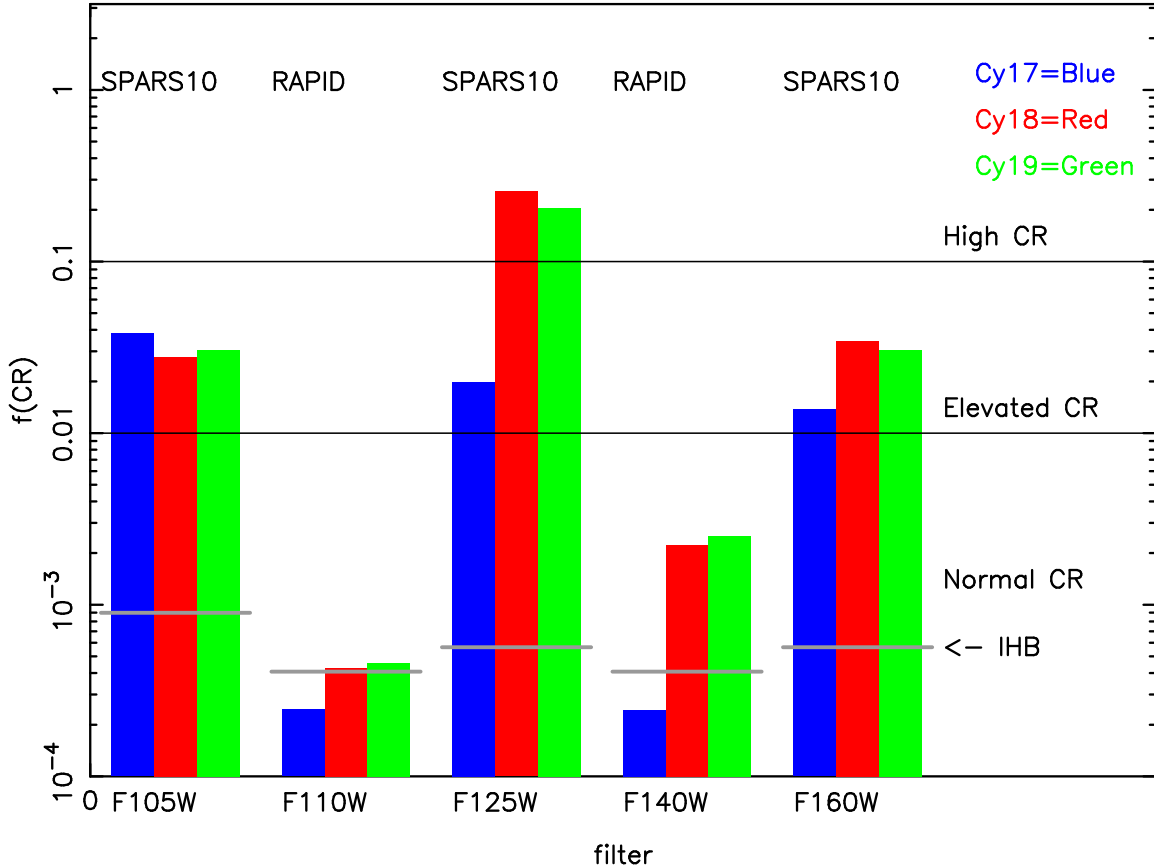


Figure 2. The fraction of pixels that are flagged as being hit by CRs for the five broad band filters used for the internal flat field program. Expected fractions are shown with gray horizontal bars. It is clear that filters using the SPARS sampling sequence have significantly higher fraction of pixels flagged as CR hit compared to what is expected.

Illumination Pattern

Figure 3 shows the illumination pattern for the five broad band filters for Cycle 17 (left panels) together with ratio images for which the internal flat fields for Cycle 17 has been divided by the Cycle 18 and 19 images (two mid panels) and Cycle 18 divided by Cycle 19 (right panels). The illumination pattern appears to be stable over the Cycles, with no apparent gradients appearing, except possibly for F125W. In this filter, it is likely the large difference in the number of CR flagged pixels between Cycle 17 and Cycles 18 and 19 that causes a slight variation in the flat field structure. Inspecting the filters without the excess of false CR flags, i.e., F110W and F140W, reveals no significant gradients. To the bottom right of the detector, there are, however, some features visible in the ratio images, including the “wagon wheel” feature. The features are slightly more prominent in the F140W filter compared to F110W. For the F140W filter, the strength of the features is in

the range 0.1%-0.5%, in the sense that the pixels in the latter epochs show a higher signal in these areas compared to Cycle 17. The ratio images between Cycle 18 and Cycle 19 shows very little structure. This is expected since the same observational ordering between filters was used in these two cycles, minimizing effects due to image persistence.

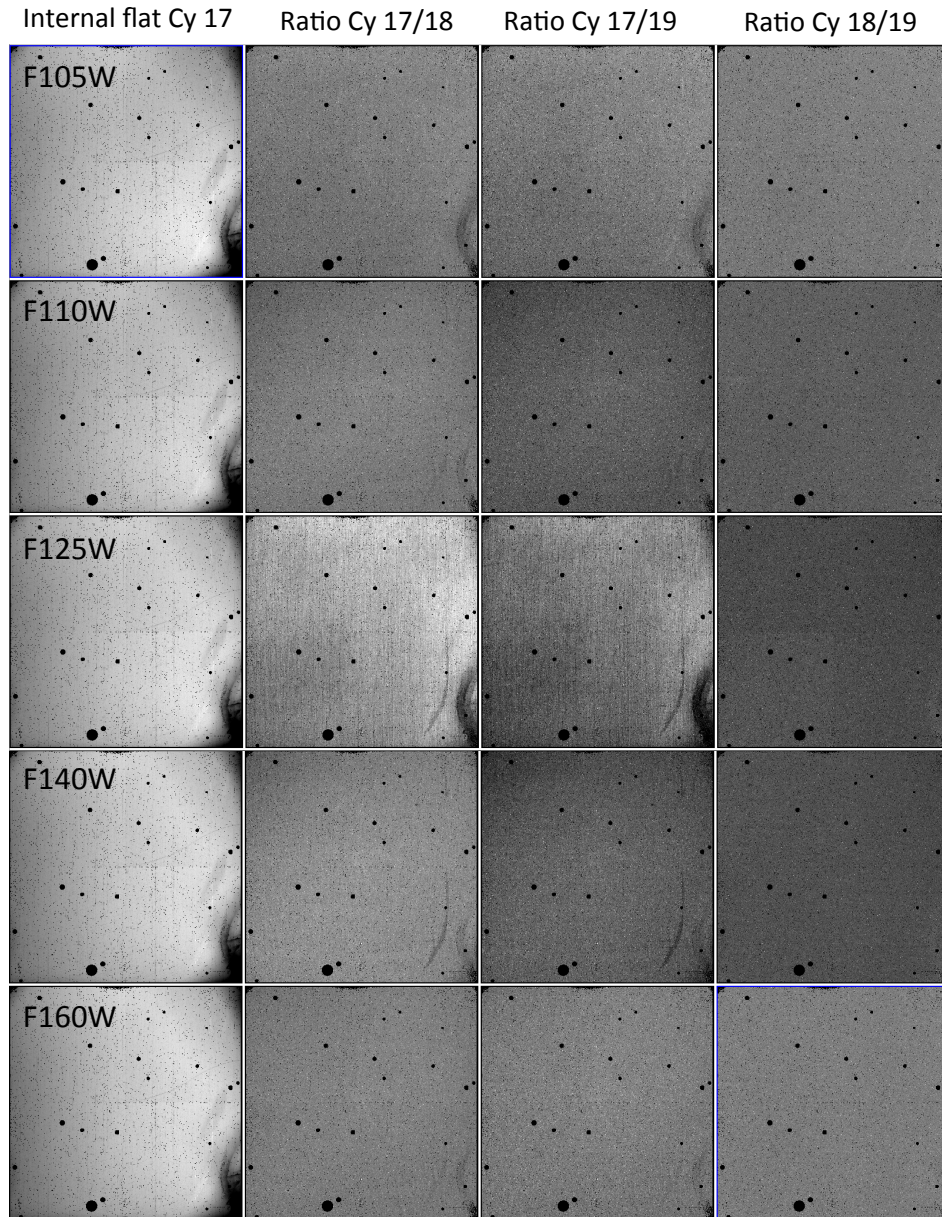


Figure 3. **Illumination patterns for the five IR broad band filters: F105W, F110W, F125W, F140W, and F160W.** Panels in left column show the Cycle 17 flat field illumination pattern, while the remaining columns show the Cycle 17 flat field image divided by the Cycle 18, the Cycle 17 image divided by the Cycle 19 image, and the Cycle 18 image divided by the Cycle 19 image, respectively. Black circles show pixels that are masked (the “death star” and IR “blobs”).

Figures 4 and 5 show the flat field images for the remaining ten narrow and medium band filters. Again, the ratio images show that the structure is stable across cycles. However, since all narrow and medium band internal flat field images were taken using the SPARS sampling sequence, we can expect some structure due to the false flagging of CRs. Furthermore, since the Cycle 18 and 19 observations only consist of 2-3 individual exposures, they are more likely to be affected by image persistence from exposures taken prior to the calibration images. In fact, a number of filters show signs of persistence consistent with preceding grism observations (F128N, F167N).

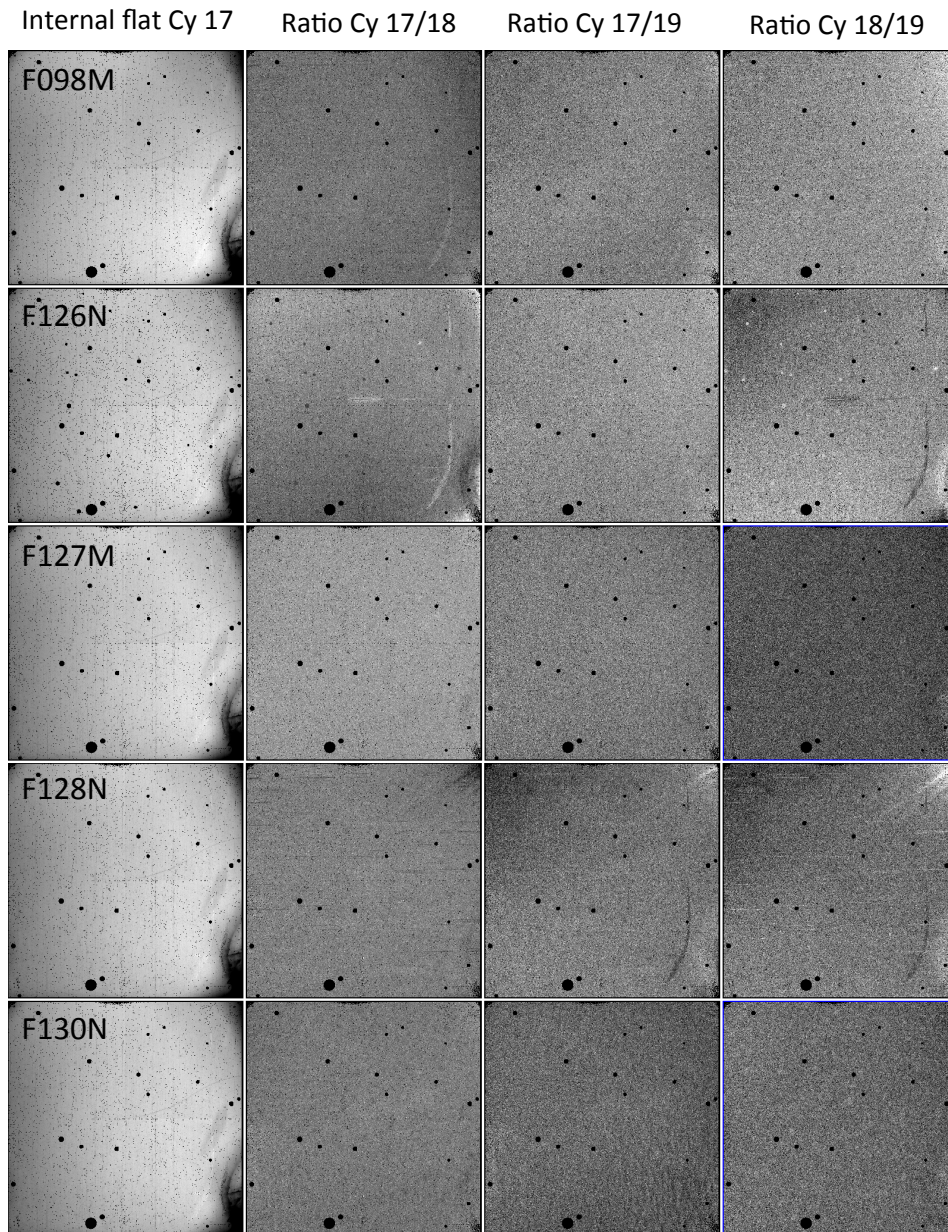


Figure 4. Illumination patterns five IR narrow and medium band filters: F098M, F126N, F127M, F128N, and F130N. Left panels show the Cycle 17 flat field illumination pattern, while the remaining columns show ratio images between the different Cycles.

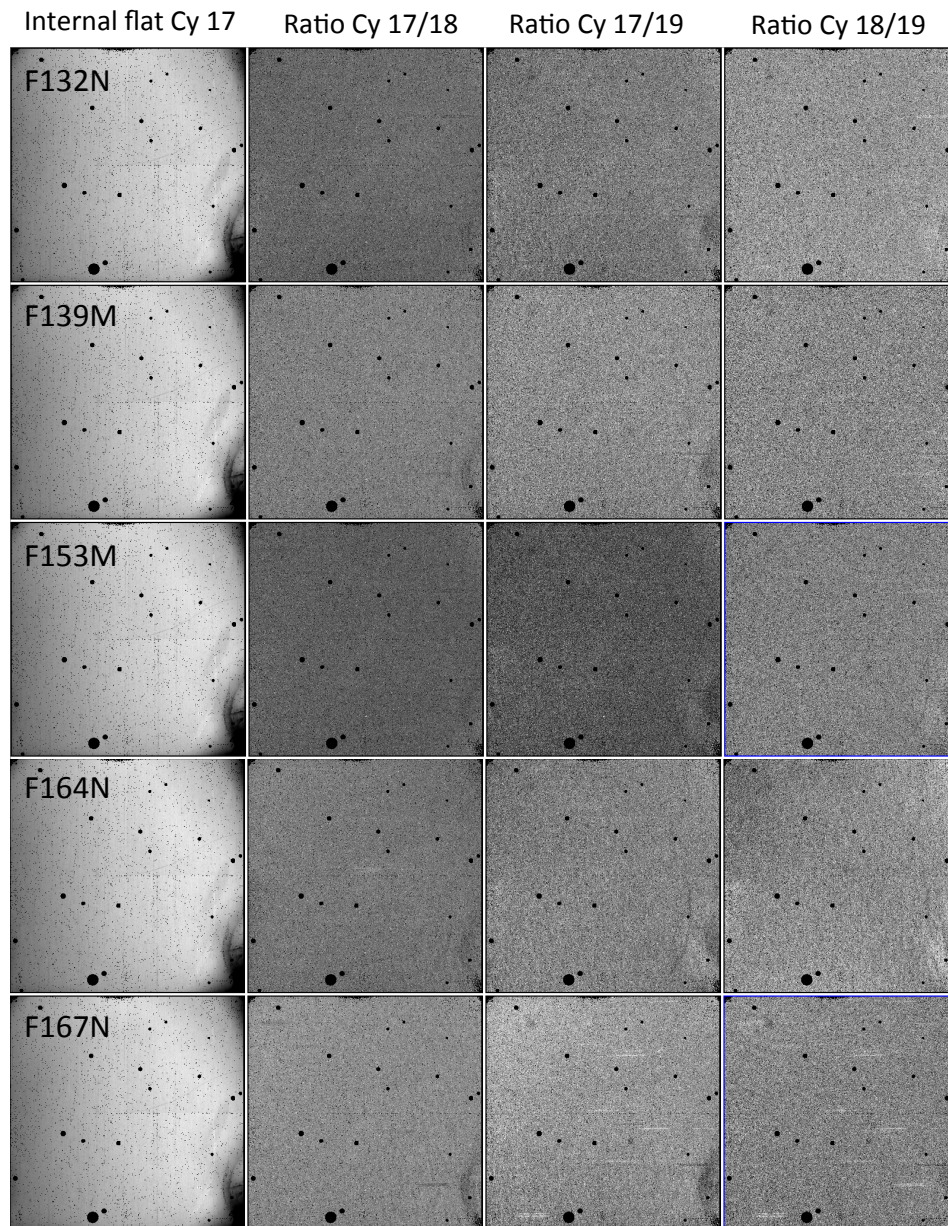


Figure 5. Illumination patterns for five IR narrow and medium band filters: F132N, F139M, F153M, F164N, and F167N. Left panels show the Cycle 17 flat field illumination pattern, while the remaining columns show ratio images between the different Cycles.

To illustrate the difference in illumination pattern between the TV3 testing on ground and the inflight flight observations, we plot in the top panels of Figure 6 the shape of the flat

fields from ground (left) and from Cycle 17 (right) in the F160W filter. The stretch used in the figure is $\pm 10\%$ in intensity.

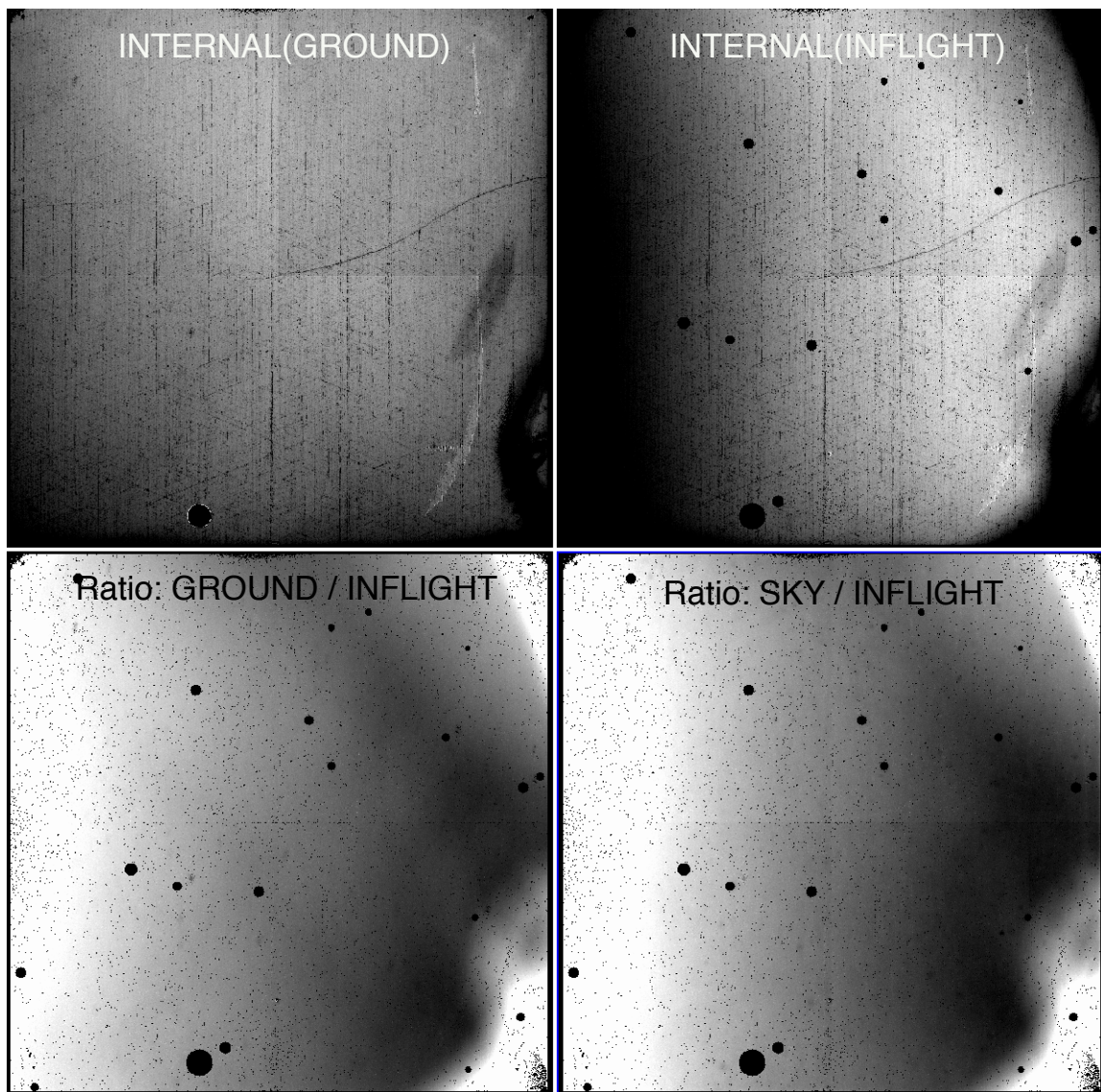


Figure 6. Top panels show the illumination pattern for the TV3 ground based internal flat field images (left) and the in-flight Cycle 17 internal flat field images (right). Bottom left panel shows the ratio of the ground based and the in-flight based internal flat fields. Bottom right panel shows the ratio between the sky flat field images and the in flight internal flat field images. All panels have a stretch $\pm 10\%$. Circles and individual black dots show bad pixels.

It is clear from the figure that there are low frequency gradients in the flat fields in addition to a number of artifacts, e.g., the wagon wheel at the bottom right. Comparing the TV3 and in-flight images shows some significant differences in the illumination, especially around the edges of the detector. The lower illumination of the in-flight flat

fields around edges and particularly the corners should be due to vignetting, i.e., blocking of a fraction of the light along the optical path. To further compare the ground based and inflight based internal flats, we plot in the lower left panel the ratio image between these two. The difference in illumination patterns between the two is clearly illustrated. Finally, in the lower right panel we show the ratio between the sky flat field image and the internal lamp flat field from the inflight calibrations. Here the former represents the flat field that should be applied to the illumination pattern from actual science observations. It is clear that the internal flat field deviates significantly from the expected illumination pattern of the sky (note that stretch is $\pm 10\%$). Therefore, the internal flat field images are not well suited for creating actual calibration flat field images. As noted above, sky images are used to create flat field images for the IR channel (Pirzkal et al. 2011).

Bad Pixels

For the WFC3 IR detector, a "bad pixel" is the name assigned to a pixel that is dead, unstable, affected by IR blobs or has an inconsistent zeroth read value. All bad pixels are listed in the bad pixel table, which is added to the data quality extension of the calibrated data, making it possible for users to exclude pixels for which data are questionable. To examine the health of individual pixels and to determine which are bad, calibration programs taking internal darks and flat fields are used. A detailed description of the creation of the latest bad pixel table is given in Hilbert (2012). In summary, the F140W internal flat field images taken during Cycles 17 to 19 were used to determine bad pixels in two categories. First, all pixels with zero or negative response, or that have a response less than 30% of the surrounding local pixels, were classified as dead pixels. Secondly, individual pixels that showed a significant temporal (i.e., the pixel value in an individual image deviating more than 5σ from the mean value of that pixel) or spatial variation (any pixel with an rms in the in the up-the-ramp response between multiple images that deviates by more than 7σ from the mean of the rms of the whole detector) were considered unstable and therefore also assigned a bad pixel flag. Adding pixels that were flagged from the investigation of dark images, as well as pixels affected by IR blobs (see below) and the death star, results in a total of 28,500 pixels that are flagged as bad in the IR detector (about 2.8% of all pixels). Note that we in the investigations in the previous sections have excluded pixels flagged as bad when examining the overall behavior of the detector response in the different filters.

IR blobs

Small blemishes, dubbed “IR blobs” have been detected on IR images after the installation of WFC3 during Servicing Mission 4. The IR blobs, currently about 40 of them, are regions with radii of about 10-15 pixels where the detector response is about 10-15% lower compared to the surroundings. The likely reason for the IR blobs is particles on the mirror of the Channel Select Mechanism (CSM), which diverts the incoming light into the IR channel. The light from the internal flat field lamps does not pass via the CSM, therefore the internal flat field images cannot be used to monitor or characterize the IR blobs. Instead flat fields constructed from sky images and dark Earth flat fields have been used to investigate these. For more information on the IR blobs see Pirzkal et al. (2010; 2012)

Conclusions

We have investigated the properties of the WFC3/IR internal flat fields obtained with the Tungsten #2 flat field calibration lamp during HST Cycles 17 to 19. In addition, to study any longer term changes in the lamp illumination, we also included images from the on ground Thermal Vacuum 3 testing and the SMOV4 in the investigation. We find, consistent with previous investigations, that the intensity of the lamp increased by ~8% between the on ground testing and the in flight measurements. We find that the intensity of the lamp has not changed significantly over the period from SMOV 4 (July 2009) to Cycles 17 through 19 (up to September 2012). We do, however, detect an internal scatter between Cycles and filters of about 0.4%, which is larger than expected from statistical errors only. There are a number of possible factors contributing to this systematic effect. These include variations in the flat field lamp output, effects due to image persistence and possible systematic effects due to an excessive flagging of pixels as being hit by cosmic rays in the up-the-ramp fitting for images with high count rates.

We do not find any significant change in the illumination pattern over Cycles 17 through 19. There may, however, been some small changes in the response in the pixels in some areas in the bottom right of the detector (e.g., the wagon wheel feature). There is a significant difference in the illumination pattern between the internal flat field images and the sky flat field images, suggesting that the latter cannot be used to create accurate flat field calibration files.

Acknowledgements

The author is thankful to Bryan Hilbert for reviewing and commenting on this ISR.

References

Baggett, S., Sabbi, E., & McCullough, P. 2009, WFC3 Instrument Science Report, WFC3-ISR - 2009-27 (Baltimore:STScI)

Bushouse, H. 2008, WFC3 Instrument Science Report, WFC3-ISR - 2008-28 (Baltimore:STScI)

Hilbert, B. 2012, WFC3 Instrument Science Report, WFC3-ISR - 2012-10 (Baltimore:STScI)

Long, K. S., Wheeler, T., & Bushouse, H. 2011, WFC3 Instrument Science Report, WFC3-ISR - 2011-09 (Baltimore:STScI)

Pirzkal, N., & Hilbert, B. 2012, WFC3 Instrument Science Report, WFC3-ISR - 2012-15 (Baltimore:STScI)

Pirzkal, N., Mack, J., Dahlen, T., & Sabbi, E. 2011, WFC3 Instrument Science Report, WFC3-ISR - 2011-11 (Baltimore:STScI)

Pirzkal, N., Viana, A., & Rajan, A. 2010, WFC3 Instrument Science Report, WFC3-ISR - 2010-06 (Baltimore:STScI)

Powers, C., Materials Engineering Branch, Code 541, NASA Goddard Spaceflight Center, Greenbelt, MD 20771, priv.comm., Feb 2013.